JOURNAL OF SPACECRAFT AND ROCKETS
Vol. 44, No. 3, May–June 2007

Plume Impingement Analysis for Aeolus Spacecraft and Gas/Surface Interaction Models

Gennady N. Markelov*
Advanced Operations and Engineering Services Group, B.V., 2300 AH Leiden, The Netherlands

DOI: 10.2514/1.24425

A numerical analysis of plume impingement onto solar arrays of the Aeolus spacecraft was performed for plumes exhausted from a single thruster or four thrusters simultaneously. Spacecraft configurations with stowed and deployed solar arrays were considered. The arrays were located at large angles from the thruster centerline or at a large distance from the thrusters. Therefore, for both configurations, all flow regimes were expected, from continuum through transitional to free-molecular. To perform the analysis, a multizone approach was used. It applied a solution of Navier–Stokes equations in the thruster nozzle and near-plume field and applied the direct simulation Monte Carlo method for plume impingement. Results showed that the plume effects were affected by chemical composition and the thruster vector. A flow near the solar array surface was almost free-molecular and a gas/surface interaction was very important to provide reliable results. Several gas/surface interaction models, diffuse reflection, and different versions of the Nocilla model were used to compute the plume impingement effects. Those versions used model parameters obtained for orbital conditions with high molecular velocities and plume impingement with moderate molecular velocities.

Nomenclature

F	=	force, N
f	=	reduced force coefficient
k	=	Boltzmann constant, $k = 1.38066 \times 10^{-23}$ J/K
M	=	torque, N · m
m	=	molecular mass, kg
n	=	density
p	=	force or impulse of molecule
S	=	velocity ratio, $S = V/\sqrt{2(k/m)T}$
T	=	temperature, K
v	=	velocity, m/s
X, Y, Z	=	Cartesian coordinates, m
θ	=	angle between velocity vector and surface normal, deg

Subscripts

i	=	incident molecules
n	=	normal component
s	=	scattered molecules
t	=	tangential component
w	=	wall

I. Introduction

THE Aeolus spacecraft is the second of ESA's Earth Explorer core missions. It will provide a global observation of three-dimensional wind fields over the Earth's surface. This significantly enhances the current observation capabilities and improvement in atmosphere modeling, especially in the area over oceans, tropics, and southern hemispheres. In addition, Aeolus will supply information about cloud-top altitude, aerosols, and dust in the atmosphere. This is crucial for numerical weather prediction and, in particular, for climate studies. Observations will be performed with an ALADIN instrument that uses the active Doppler wind lidar method. Development of the Aeolus spacecraft began in 1999, and 50 space companies in 12 European countries supplied various equipment and services for the mission. The Aeolus spacecraft is based on the Mars/Venus Express platform design, and it has a launch mass of about 1.5 tons and an expected total lifetime of 3.25 years. It is planned to launch the spacecraft in a sun-synchronous dawn-to-dusk orbit at an altitude of 400 km in October 2008.

For orbital maneuvers, Aeolus employs a monopropellant hydrazine propulsion system. The spacecraft has ten 5-N thrusters arranged in two redundant branches. Four pairs of thrusters are mounted on the leeward side ($-X$ face) of the spacecraft (Fig. 1) to provide drag compensation and three-axis torque control. Plumes exhausted from the thrusters interact with the solar arrays, causing mechanical and heat loads and contamination on the solar array surfaces. Radiators mounted on the $-X$ side of the spacecraft body are contaminated and heated by a plume backflow. Therefore, an accurate and reliable prediction of plume impingement effects is very important for the orbit operations and the lifetime of Aeolus. This paper presents numerical results for heat and mechanical loads on the solar arrays only. A gas/surface interaction model is important for the case under consideration, and the plume impingement analysis was performed using simple and advanced models to study their influence on the numerical solution. The advanced model was applied with the model parameters obtained for orbital conditions with high molecular velocities and plume impingement with moderate molecular velocities.

II. Aeolus Spacecraft Geometry

Figure 2 shows simplified geometries of Aeolus with stowed and deployed solar arrays (SAs). Only half of the Aeolus geometry with a solar array in the $-X$ direction was considered to model the interaction of thruster plumes with the solar array and the spacecraft surface. Axis Z is a vertical centerline of the spacecraft, and the bottom of the spacecraft box is at $Z = 0.2$ m. The geometries are created with a geometry subsystem of SMILE [1] software in accordance with [2]. Each geometry consists of more than 66 primitives such as a circle, cone, cylinder, rectangle, etc. The primitives are divided into more than 90,000 triangles, with a length scale for each triangle of between 1 and 2 cm. The triangles are used to model collisions of molecules with the surfaces and to sample forces, torques, and heat fluxes. The center of gravity is assumed to

Presented as Paper 5067 at the 38th AIAA Thermophysics Conference, Toronto, Ontario, Canada, 6–9 May 2005; received 4 April 2006; revision received 30 November 2006; accepted for publication 30 November 2006. Copyright © 2007 by G. N. Markelov. Published by the American Institute of Aeronautics and Astronautics, Inc., with permission. Copies of this paper may be made for personal or internal use, on condition that the copier pay the $10.00 per-copy fee to the Copyright Clearance Center, Inc., 222 Rosewood Drive, Danvers, MA 01923; include the code 0022-4650/07 $10.00 in correspondence with the CCC.

*Senior Aerospace Engineer, Postbus 342; Gennady.Markelov@aoes.com. Member AIAA.

Fig. 1 An artist's view of the Aeolus spacecraft (courtesy of MediaLab and Advanced Operations and Engineering Services Group, B.V.).

be $X = 0.016$ m, $Y = 0.006$ m, and $Z = 1.087$ m for both configurations, despite that its location can be changed during the mission.

III. Thruster Parameters

The propulsion system is based on ARC MONARC 5-N thrusters that have a bell-nozzle profile with throat and exit diameters of 1.98 and 23.1 mm,[†] respectively. The thruster can operate at different chamber pressures, and in the present paper, chamber pressure and temperature are equal to 8.3 bar and 700°C, respectively. A level of ammonia dissociation for the thruster is 50–70%. However, plume analysis is performed for two sets of chemical composition (Table 1). The first set corresponds to almost complete dissociation, in accordance with [3], for the considered chamber conditions, and the second one is obtained assuming 60% dissociation of ammonia. These two sets allow one to estimate the effect of an uncertainty in ammonia dissociation applied in the numerical prediction. The first case is also useful to study an application of gas/surface interaction models, because there is a lack of information for NH_3 and the first set includes a negligible amount of ammonia. The following sections show results obtained for a branch of thrusters that have the closest location to the solar array. The coordinates and thruster vectors of these thrusters are listed in Table 2. It is assumed that the origin of the thruster local coordinate system is at the nozzle throat.

Table 1 Mass fractions

Set	H_2	N_2	H_2O	NH_3
1	0.1052	0.8839	0.001	0.00086
2	0.07425	0.63528	0.001	0.28046

Table 2 Thruster locations and vectors [2]

Thruster	Location, m			Direction cosines		
	X	Y	Z	X	Y	Z
1	−0.8374	0.6299	0.350	−0.9659	0.2588	0.0
2	−0.8374	−0.6299	0.350	−0.9659	−0.2588	0.0
3	−0.8374	0.6299	1.800	−0.9659	0.2588	0.0
4	−0.8374	−0.6299	1.800	−0.9659	−0.2588	0.0

IV. Numerical Approach

Plumes exhausted from Aeolus thrusters impinge the SA, which can be in stowed or deployed positions. The stowed SA locates close to the thruster nozzle but at large angles (more than 60 deg) from the thruster centerline. A deployed SA is at a very large distance from the thruster, and a side portion of the thruster plume interacts with the SA. Plume properties at large angles from the thruster centerline are defined mainly by the parameters of a boundary layer formed on the nozzle wall. Therefore, flow properties have to be resolved properly in any part of a computational domain for an accurate numerical prediction of plume effects. For a plume expanding into a vacuum, the entire range of the flow regimes is observed, from the continuum flow inside the nozzle to the transitional and free-molecular at large distances from the nozzle. This requires a special numerical approach to obtain a solution that is physically reliable near the spacecraft body and the solar array. The simulations must be performed for very large spatial scales (hundreds of nozzle diameters) to determine the plume effects on the solar arrays.

A multizone approach was successfully used for plume impingement analysis [4,5], and it implies the partition of the flowfield into several zones, based on the flow rarefaction degree. The flow in the first zone (inside the nozzle and near vicinity) is continuum, and the solution here is obtained by solving the Navier–Stokes (NS) equations. The results of the NS computation are used as input conditions for the second zone, which expands downstream from the first zone and includes the spacecraft surface. The direct

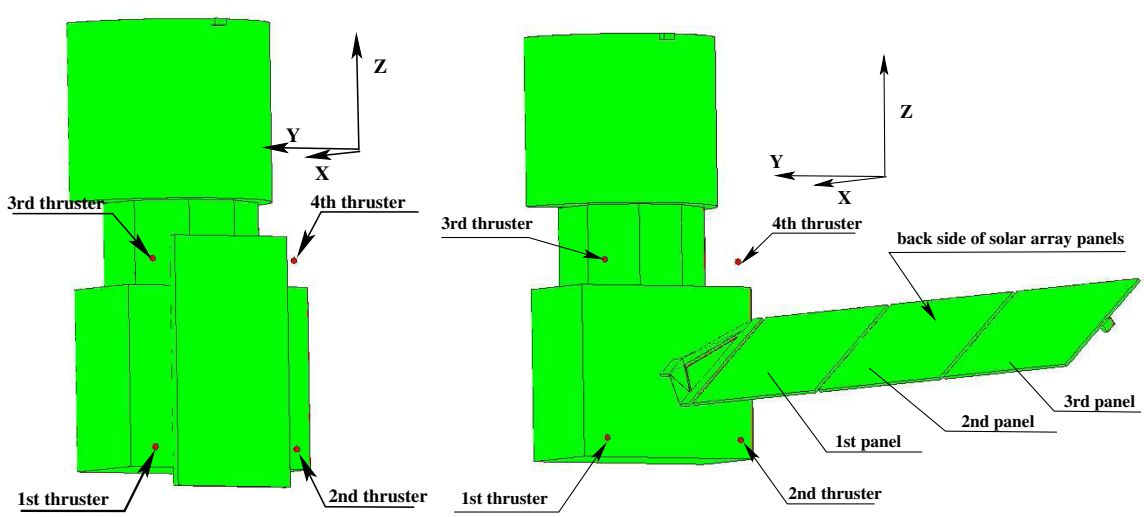

a) Stowed solar array **b) Deployed solar array**

Fig. 2 Aeolus spacecraft geometries.

[†]Data obtained via private communication with R. Brandt in 2004.

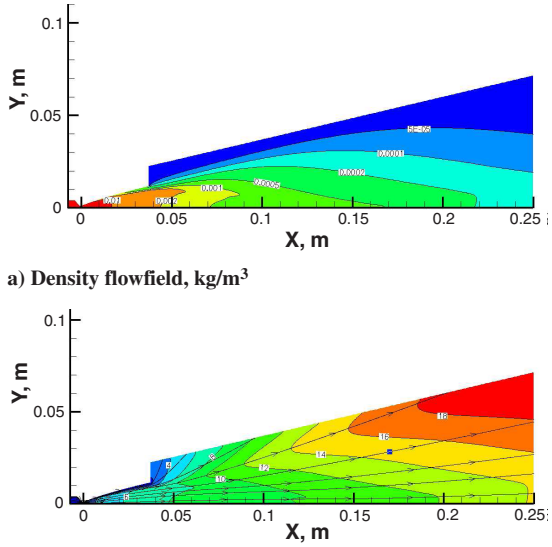

a) Density flowfield, kg/m^3

b) Mach number flowfield and selected streamlines

Fig. 3 Nozzle flow and near-plume field (NS results, set 1).

simulation Monte Carlo (DSMC) method [6] can be applied here in 3-D formulation, or the second zone could be subdivided further into a few subzones (in this paper, into two subzones) to speed up and simplify computation. In the latter case, axisymmetric and 3-D formulations are used for the first and second subzones, respectively. The specific time step and numbers of model particles and cells are applied for each subzone. An ellipsoidal Maxwellian distribution function with different temperature values along the Cartesian coordinates is used to sample particles entering a subzone, because it preserves the flow thermal nonequilibrium through a subzone boundary.

V. Nozzle Flow and Near-Plume Field

A simulation of the nozzle flow and near-plume field was performed with CFD-FASTRAN [7], which is a compressible finite-volume Navier–Stokes solver. Roe's flux difference upwind scheme was used. The Van Leer *minmod* limiter was applied to provide the second-order spatial accuracy. The flow was a mixture of perfect gases, the parameters of which are determined in the FASTRAN database. The nozzle wall was assumed adiabatic and no-slip boundary conditions were applied. A computational domain was extended as far as possible downstream from the nozzle exit plane to include regions with continuum and partially transitional flow regimes, and fixed-pressure boundary conditions were imposed at outflow boundaries. The pressure was 1 N/m^2 and it was used during a transient period of a computation until a flow became supersonic at the boundary. Then the solver used extrapolation boundary conditions automatically. The computations were performed for three structured multiblock grids to confirm the solution convergence. The fine grid has 641×113 nodes along the nozzle axis and radius inside the nozzle, and the total number of nodes is about 125,000, including the near-plume field. Nodes are clustered to the nozzle wall and in the vicinity of the throat. Figure 3 shows the nozzle flow and the near-plume field structure obtained with the fine grid. For the considered chamber conditions, numerical solutions predict a thrust F_T of 4.209 and 4.302 N for the first and second sets of chemical compositions, respectively.

VI. Plume Impingement

Axisymmetric and 3-D versions of the DSMC software SMILE [1] are used for kinetic simulations of plume flow and plume impingement, respectively. SMILE is based on the majorant frequency scheme of the DSMC method. The software has advanced models for real gas effect and chemical reactions and efficient numerical techniques and algorithms to speed computations up. For the present analysis, the variable hard-sphere model was used as the intermolecular-collision model, and the Larsen–Borgnakke model with temperature-dependent relaxation numbers was applied to redistribute the energy between translational and internal energy modes.

DSMC results presented in this section were obtained using diffuse reflection with complete energy accommodation as a gas/surface interaction model. The wall temperature was assumed constant and equal to 167 or 273 K. The first value is the lowest estimate of the wall temperature of a shadowed surface. A numerical accuracy of DSMC solutions is discussed in the Appendix.

A. Stowed Configuration

NS results are used as inflow boundary conditions for a 3-D computation of a flow around the configuration with stowed solar array. A position of the boundary has to be located in the continuum flow regime in which the NS equations are valid and a breakdown parameter B was used to find the position. The parameter was derived by Bird [6] for plume expansion to be used as a criterion of an applicability of a continuum approach. It is commonly assumed that the continuum approach is not valid when $B \geq 0.02$. The inflow boundary consists of two straight lines to simplify an extraction of NS results along it. The distance between the thruster nozzle lip and the solar array is rather small, and it is not possible to split the second (DSMC) zone into subzones. For instance, some molecules reflected from the edges of the solar array affect flow properties at a distance of one exit diameter from the inflow boundary. Figure 4a shows temperature isolines obtained with and without solar array, in which the X axis is the plume centerline. The reflected molecules could penetrate so closely to the nozzle lip because the flow is rather rarefied in the region between the lip and the solar array. The plume flow becomes transitional ($B > 0.02$), then almost free-molecular ($B > 1$) at some distance from the nozzle lip, and again becomes transitional in the vicinity of the solar array (Fig. 4b).

Table 3 shows that forces and torques due to plume impingement are very small for both sets of chemical compositions, because only a small portion of the plume (an angle from the plume centerline is more than 65 deg) interacts with the solar arrays. Distributions of convective heat fluxes over the Aeolus spacecraft surface are shown in Fig. 5 for the first and third thrusters. Stowed solar array panels are considered as one body and the maximum heat fluxes listed in Table 4 are taken at 1/3, 2/3, and 3/3 of the body edge thickness. The highest value is about 350 W/m^2. Incomplete dissociation of ammonia increases a fraction of lightweight species and changes flow properties inside the nozzle and in the plume. Note that the number density in the side portion of the plume is almost unchanged for the considered sets, whereas gas impulse and energy increase with incomplete dissociation. This leads to higher values of disturbing forces and torque (which are more important for the configuration with deployed solar array) and heat fluxes. The latter increases by 25% for the case under consideration.

The flow between the thruster and solar array edges has a complex structure on a relatively small spatial scale. Neglecting intermolecular collisions leads to very different flow properties in this region; however, heat fluxes onto the solar array edges are in good agreement with the DSMC solution. One of the goals of the performed analysis was a computation of heat and mass fluxes onto radiators mounted on the $-X$ wall of the spacecraft and an application of the free-molecular approach was not successful for a prediction of these fluxes.

B. Deployed Configuration

A solar array panel is about 2-m long, and the distance between the thruster and the tip of the third panel of the solar array is about 7 m. This is much larger (by a factor of 45) than a corresponding distance for stowed solar array. An enlargement of the computational domain used for the stowed solar array configuration requires significant increase of computer resources. Computations of the stowed array configuration were performed at the limit of available resources, and

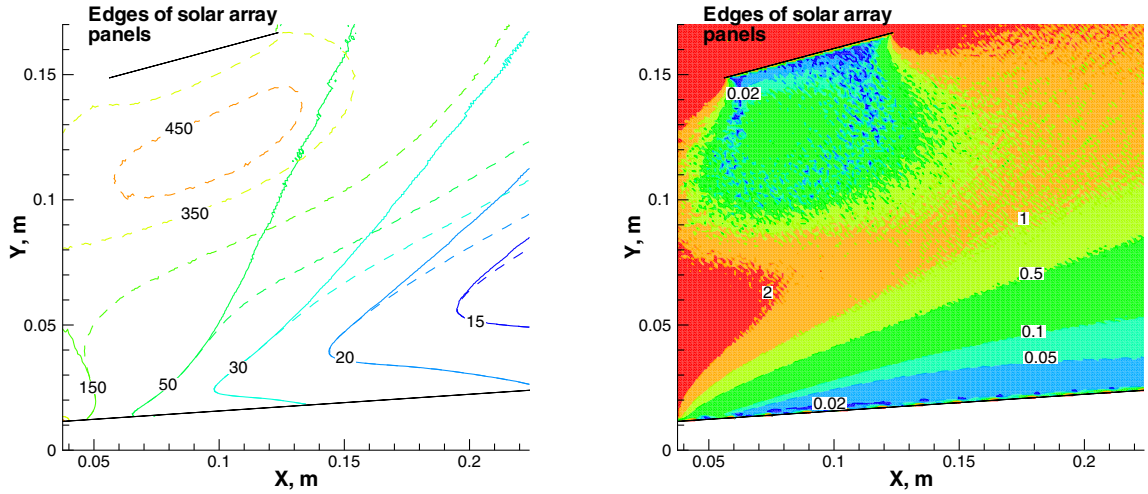

a) Translational temperature isolines, K; without solar array (solid line) and with solar array (dashed line)

b) Breakdown parameter flowfield

Fig. 4 Flow in the vicinity of the solar array and thruster (set 1, axisymmetric DSMC results, and $T_w = 273$ K).

this approach cannot provide accurate solution now. Therefore, the DSMC zone is subdivided into two subzones: an axisymmetric plume and 3-D plume impingement.

1. Axisymmetric DSMC Results for the Plume

The first subzone extends up to a distance of 1 m from the nozzle exit plane along the plume centerline and up to only 0.1 m in the radial direction. The sizes are chosen such that the outflow boundary will serve as the inflow boundary for successive 3-D computations, and flow parameters along the boundary must not be affected by molecules reflected from the Aeolus spacecraft surface. An inflow boundary of the first subzone is the boundary used for the computations of flow around the configuration with stowed solar array. Figure 6 shows axisymmetric DSMC and NS solutions for a near-plume field. A density predicted by both methods coincides with each other in all overlapped domains, and the Mach number begins to deviate at breakdown parameter values of 0.07–0.08. For a plume impingement analysis, a boundary between the continuum and transitional regimes is taken by most researchers as $B = 0.05$ (see, for example, [5,8,9]). As mentioned in [6], the initial breakdown of the continuum approach starts at approximately $B = 0.02$, and for the case under consideration, a difference between rotational and translational temperatures reaches 3 and 5% at $B = 0.05$ and 0.08, respectively.

2. Three-Dimensional DSMC Results

This section presents results obtained for the second subzone that includes spacecraft geometry. Figures 7 and 8 show a density flowfield and convective heat flux distribution over the Aeolus spacecraft surface for a single thruster firing as well as for four thrusters firing simultaneously. The maximum values of heat fluxes are listed in Table 5 for the yoke and solar array panels, and forces and torques are shown in Table 6 for both sets of chemical composition. An incomplete dissociation of ammonia increases absolute values of forces and torques and the maximum values of heat fluxes.

A flow regime is near-free-molecular in the vicinity of the solar arrays, but intermolecular collisions are still important. Therefore, the firing of a few thrusters produces forces and torques that are different from the sum of corresponding effects from single thrusters. For example, four thrusters produce F_X higher by 14% than the sum of F_X obtained from single thrusters. To clearly show the influence of intermolecular collisions, additional computations with switched-off collisions are performed. Neglecting intermolecular collisions (free-molecular results in Tables 5 and 6) for a single thruster increases F_X and heat fluxes, but decreases absolute values of F_Y, F_Z, and torques. For the inflow boundary used, a value of breakdown parameters varies from 0.15 to 10 in the backflow. A boundary between transitional and free-molecular regions is not well-defined as a continuum breakdown, and some researchers assume that free-molecular assumption can be applied when a mean free path approaches the size of a computational domain [8] or a value of the breakdown parameter that is significantly more than unity [5]. Free-molecular predictions of forces and torques slightly depend on the position of the inflow boundary. For example, when the boundary is moved upstream to $B = 0.02$, the forces and torques change further (about 5% of the corresponding DSMC values); however, heat fluxes decrease more significantly due to this movement (about 50%).

C. Inclination of Thruster Vector

Thrusters are inclined by 15 deg in the X–Y plane away from the solar arrays to reduce heat fluxes. This leads to an additional thrust loss of about 3.41 and 13.63% of F_T for a single thruster and for four thrusters, respectively. A small angle can also lead to significant mechanical loads and thrust loss, because the plume interacts strongly with the solar array. Computations with a zero-inclination angle show that heat fluxes can be increased by a factor of 3–7 for both configurations (Tables 7 and 8). Forces and torque are increased significantly, however, they are still negligible for the stowed array configuration (Table 9). For the deployed array, plumes exhausted from thrusters 1 and 4 produce smaller total thrust loss than for 15 deg inclination (Table 10). The thrust loss is higher for thrusters 2 and 3; those plumes interact with the face and back sides of the solar array.

Table 3 Forces and torques (stowed configuration; $T_w = 167$ K and $M = F_T \times 1m$)

Set	Thruster	F_X/F_T, %	F_Y/F_T, %	F_Z/F_T, %	M_X/M, %	M_Y/M, %	M_Z/M, %
1	1	0.0417	−0.1701	0.0400	−0.0999	0.0116	0.1288
1	3	0.0012	−0.1895	−0.0426	0.1097	−0.0361	0.1723
2	1	0.0330	−0.1930	0.0423	−0.1152	0.0200	0.1555
2	3	−0.0075	−0.2117	−0.0455	0.1235	−0.0450	0.1982

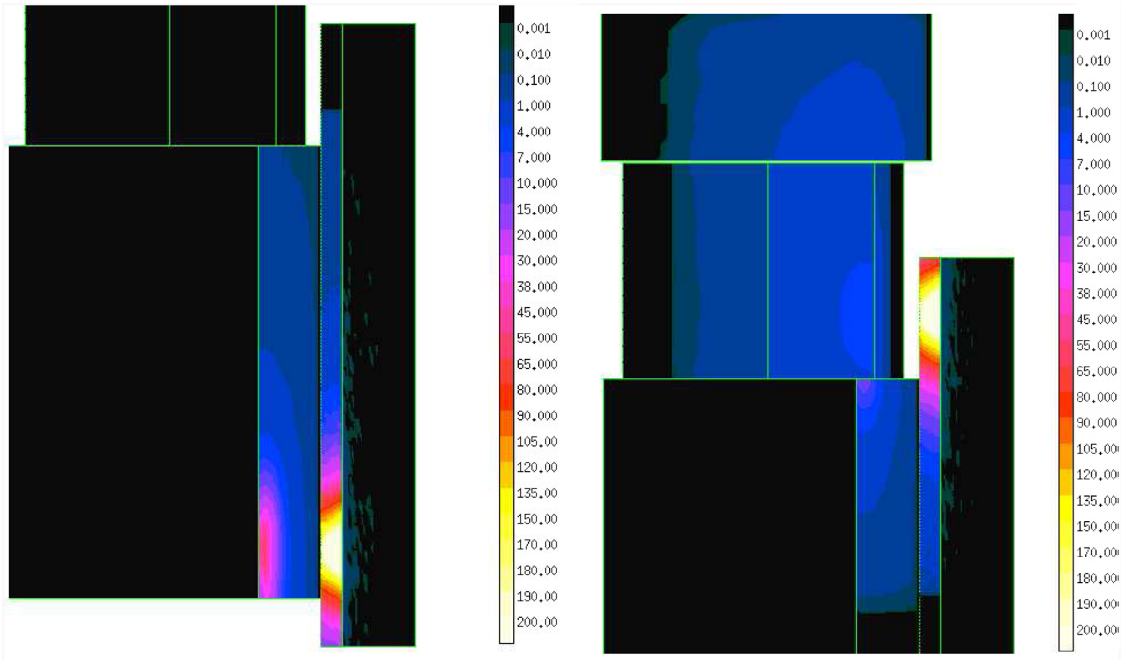

a) Thruster 1 b) Thruster 3

Fig. 5 Convective heat fluxes (values in W/m^2, stowed configuration, set 1, and $T_w = 167$ K).

Additional computations for the thruster 2 reveal that the thrust loss has a minimum of around 10 deg and this minimum is 90% of the thrust loss at 15 deg. In this case, heat fluxes are about 40 and 80% higher than the corresponding values for the 15-deg case for SA sides and edges, respectively.

VII. Influence of a Gas-Surface Interaction Model

A flow is almost in free-molecular regime near the spacecraft surface, and collisions of molecules with the spacecraft surface play a dominant role. As a result, an accuracy of plume impingement analysis depends strongly on a gas/surface interaction model that defines velocities of scattered molecules. The simplest model is diffuse reflection. This model is widely used to estimate maximum heat fluxes, applying a complete accommodation of energy. This model is also applied to predict forces and torques. In this case, it is assumed that there is no energy accommodation at all. A velocity vector of reflected molecules is defined from diffuse reflection, however, its value is not changed. To more accurately describe gas/surface interaction, a number of models were developed, for example, specular-diffuse, Nocilla [10], and Cercignani–Lampis–Lord (CLL) [11], to be used for the DSMC method. They allow simple and advanced analytic representations of the distribution function of scattered molecules. The Nocilla and CLL models handle a distribution function with lobular shape.

The following sections present results obtained from diffuse reflection with and without energy accommodation and the Nocilla model. The Nocilla model is based on experimental data; for example, it provides incomplete energy accommodation. Therefore, diffuse reflection results represent limiting cases, compared with the Nocilla model results. A study of the influence of a gas/surface interaction model was done for the deployed SA configuration and for set 1 of chemical composition.

Table 4 Maximum convective heat fluxes over solar array panels, W/m^2 (stowed configuration; $T_w = 167$ K)

Set	Thruster	1 SA	2 SA	3 SA
1	1	200	230	280
1	3	200	240	285
2	1	250	310	345
2	3	270	320	355

A. Wall Temperature and Energy Accommodation for Diffuse Reflection

A computation with $T_w = 167$ K was performed for thruster 3. Changing the wall temperature from $T_w = 167$ K to 273 K increases absolute values of forces and torques, because they are mostly determined by parameters of scattered molecules (Table 11). Obviously, an increase of wall temperature leads to smaller convective heat fluxes. For the considered increase of wall temperature, a maximum difference in heat fluxes is about 20% (Table 12).

Reference [12] shows that a diffuse reflection without energy accommodation provides a better agreement with in-flight data. A decrease of energy accommodation has the same trends as an increase of wall temperature, because in both cases, an energy of scattered molecules increases. Table 13 shows forces and torques obtained without energy accommodation (heat fluxes are zero for this model). F_Y, F_Z, and torques are increased by 50–100%, with a few exceptions for thrusters 1 and 4 (cf. Tables 6 and 13). Plumes exhausted from these thrusters impinge on the edge and the back side of the solar array and slightly on the front side. This complicates the influence of scattered molecule energy on plume effects. F_X changes significantly less than the other parameters, because incident molecules contribute more than scattered molecules to F_X.

B. Nocilla Model

Using diffuse reflection requires one to perform two sets of computations to obtain estimates of mechanical and heat loads. Moreover, maximum estimation can be very approximate, and an advanced gas/surface interaction has to be applied to obtain reliable results. The model has to take into account incidence angle, the energy of the molecule, and the properties of the spacecraft surface. Nocilla [10] has suggested that a distribution function of reflected molecules can be presented by Maxwellian distribution with a drifted velocity $\mathbf{V}$

$$f_s = n_s(2\pi kT_s/m)^{-\frac{3}{2}}\exp\{-(m/2kT_s)(\xi - \mathbf{V})^2\} \tag{1}$$

The model has five parameters: density n_s, temperature T_s, and three components of velocity $\mathbf{V}$. An equality of incident and scattered

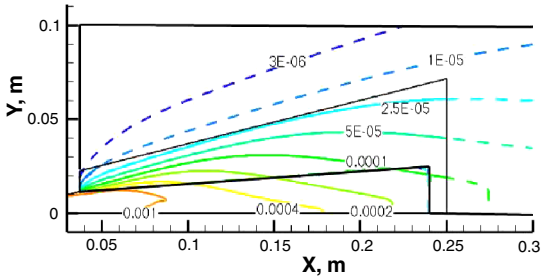

a) Density isolines, kg/m³

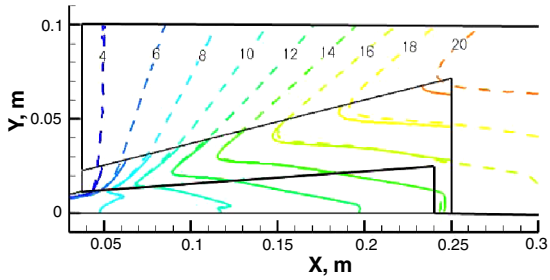

b) Mach number isolines

Fig. 6 Near-plume field (set 1, solid lines are NS results, dashed is the DSMC solution, bold black line is the boundary of the DSMC zone, and thin black line is the NS zone).

fluxes defines the density, and one of the velocity components can be removed by a proper choice of a coordinate system. For example, a component of velocity perpendicular to a plane, determined by a velocity vector of incident molecule and surface normal, is zero. The other three free parameters are obtained using experimental data and/or simplifications (see, for example, [13,14] and references therein). The following subsections discuss ways to determine the Nocilla model parameters. For the sake of simplicity, they are furthermore called models.

1. *TsAGI Model*

Many experiments for the interaction of a molecular beam with engineering surfaces typical for aerospace applications were conducted at the Central Aerohydrodynamic Institute (TsAGI) in Moscow [15,16], to determine the parameters of the Nocilla model. A beam velocity was varied from 4 to 8 km/s and molecules were N_2 and/or O_2. Forces exerted on surfaces and angular distribution of scattered molecules were measured and the following approximations were obtained:

$$p_{sn} = [a_n + b_n(2\theta_i/\pi)]p_i + \sqrt{(\pi/2)mkT_w} \tag{2}$$

$$p_{st} = -\{a_t + b_t[(2\theta_i/\pi) - (1/2)]\}p_i \sin\theta_i \tag{3}$$

Values of coefficients for solar array material and white paint are listed in Table 14.

Taking into account that a data volume is much bigger and more accurate for force measurements than for the angular distribution, TsAGI used the approximations of forces [Eqs. (2) and (3)] to determine T_s and S_t. Data obtained for angular distribution of scattered molecules was applied to define a dependence of S_n vs incidence angle:

$$S_n = 0.1 - 0.65(2\theta_i/\pi) \tag{4}$$

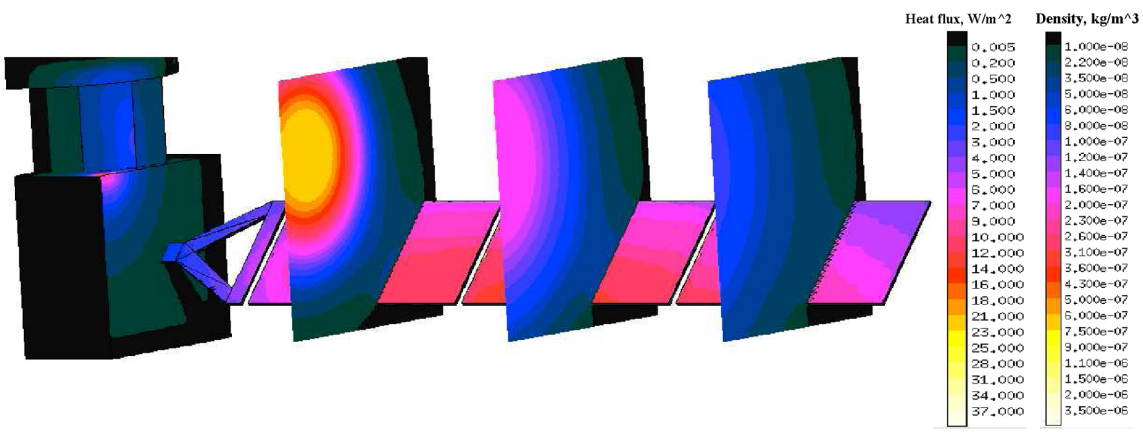

Fig. 7 Convective heat fluxes and density flowfield (deployed SA, thruster 3, set 1, and $T_w = 273$ K).

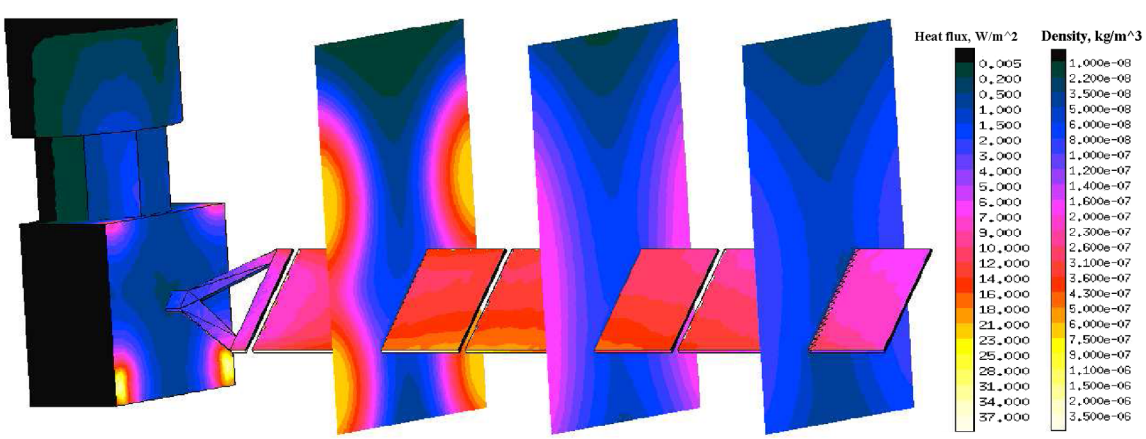

Fig. 8 Convective heat fluxes and density flowfield (deployed SA, all thrusters, set 1, and $T_w = 273$ K).

Table 5 Maximum convective heat fluxes, W/m^2 (deployed configuration; $T_w = 273$ K)

Set		Yoke			1 SA			2 SA			3 SA		
		Front	Back	Edge	Front	Back	Edge	Front	Back	Edge	Front	Back	Edge
1	1	0.3	6.1	124.3	0.3	5.5	71.0	0.3	3.3	29.7	0.2	1.3	11.1
1	2	11.0	0.1	7.8	19.0	0.01	11.3	18.9	0.01	53.5	12.1	0.01	43.1
1	3	0.02	6.0	3.3	0.01	11.9	5.0	0.01	12.9	30.9	0.01	11.0	38.1
1	4	0.04	8.4	42.7	0.2	10.2	42.2	0.2	8.4	33.8	0.1	3.7	15.0
1	All	11.0	11.5	124.2	20.5	19.3	71.5	20.8	19.0	90.7	14.7	15.0	69.7
2	1	0.4	8.1	159.9	0.7	8.2	95.1	0.7	5.0	35.6	0.4	2.0	14.7
2	2	14.9	0.02	10.4	25.3	0.01	15.2	24.5	0.01	68.2	13.2	0.01	47.1
2	3	0.1	8.9	4.9	0.01	16.2	6.8	0.01	17.2	40.9	0.01	13.1	44.5
2	4	0.1	10.8	56.7	0.3	13.5	57.9	0.3	10.2	41.7	0.2	4.1	17.1
Free-molecular results: axisymmetric DSMC results as inflow boundary													
1	3	0.01	6.1	3.2	0.01	12.4	5.1	0.01	13.9	33.5	0.0	12.5	46.4
Free-molecular results: inflow boundary near $B = 0.02$													
1	3	0.02	4.0	2.4	0.01	5.3	3.1	0.004	6.0	14.3	0.003	5.8	20.7

Table 6 Forces and torques (deployed configuration; $T_w = 273$ K and $M = F_T \times 1m$)

Set	Thruster	F_X/F_T, %	F_Y/F_T, %	F_Z/F_T, %	M_X/M, %	M_Y/M, %	M_Z/M, %
1	1	−0.2211	−0.1349	0.0687	−0.0203	0.1661	0.4533
1	2	−1.5897	0.8673	0.8827	0.0280	3.3779	−3.3612
1	3	−1.3621	−0.7132	−0.8297	−0.1380	−2.9690	2.8520
1	4	−0.3838	0.0752	−0.2362	0.0282	−0.7468	−0.1890
1	All	−4.0504	−0.0199	−0.1476	−0.1634	−0.2929	0.2397
2	1	−0.3267	−0.1739	0.0774	−0.0299	0.2136	0.6193
2	2	−1.8779	1.0416	1.0493	0.0384	4.0365	−4.0459
2	3	−1.6283	−0.8547	−0.9899	−0.1671	−3.5784	3.4574
2	4	−0.4732	0.0833	−0.2800	0.0361	−0.9059	−0.2253
Free-molecular results: axisymmetric DSMC results as inflow boundary							
1	3	−1.5018	−0.6408	−0.7924	−0.1306	−2.7939	2.5463
Free-molecular results: inflow boundary near $B = 0.02$							
1	3	−1.1720	−0.6113	−0.7298	−0.1232	−2.6191	2.4254

Table 7 Maximum convective heat fluxes, W/m^2 (stowed configuration, set 1, thruster 3; $T_w = 273$ K)

Inclination	1 SA	2 SA	3 SA
15 deg	200	240	285
0 deg	650	780	1010

Table 8 Maximum convective heat fluxes for zero inclination of thrusters, W/m^2 (deployed configuration, set 1; $T_w = 273$ K)

	Yoke			1 SA			2 SA			3 SA		
	Front	Back	Edge	Front	Back	Edge	Front	Back	Edge	Front	Back	Edge
1	9.9	46.5	845.9	21.4	62.3	690.7	13.6	27.6	149.8	4.5	8.7	47.9
2	31.4	0.1	19.1	100.4	0.02	29.8	82.7	0.03	196.1	30.0	0.04	91.2
3	0.04	14.7	8.3	0.01	69.1	12.3	0.02	70.2	157.7	0.02	37.5	106.9
4	0.2	25.8	106.4	3.3	76.7	273.0	4.1	52.2	154.7	1.9	18.9	66.5
All	31.1	59.1	862.5	103.0	120.5	400.0	85.7	108.0	370.7	37.4	51.4	181.4

Table 9 Forces and torques (stowed configuration, set 1, thruster 3; $T_w = 273$ K and $M = F_T \times 1m$

Inclination	F_X/F_T, %	F_Y/F_T, %	F_Z/F_T, %	M_X/M, %	M_Y/M, %	M_Z/M, %
15 deg	0.0012	−0.1895	−0.0426	0.1097	−0.0361	0.1723
0 deg	−0.0713	−0.4619	−0.0571	0.2969	−0.1001	0.4713

The TsAGI model has been applied extensively to calculate aerodynamic characteristics of spacecraft at low Earth orbit (LEO). The model does not require an iterative process, and it is very efficient for numerical modeling. The TsAGI model has been implemented in SMILE, and its application to an analysis of Space Station Mir aerodynamics revealed a big influence of gas/surface interaction on the aerodynamics and the station configuration that provides required properties [17].

Tables 15 and 16 present results obtained with the TsAGI model, assuming a solar array material for the front side of the solar array and white paint covers the rest of the spacecraft surface. The model prediction for single thrusters is about an average of diffuse model predictions obtained with and without complete energy accommodation. Heat fluxes are extremely small, compared with diffuse model prediction for the front side of solar arrays. For the back side, the difference between the TsAGI and diffuse models is about a

Table 10 Forces and torques for zero inclination of thrusters (deployed configuration, set 1; $T_w = 273$ K and $M = F_T \times 1m$)

Thruster	F_X/F_T, %	F_Y/F_T, %	F_Z/F_T, %	M_X/M, %	M_Y/M, %	M_Z/M, %
1	−2.4390	−0.9698	0.4177	−0.2400	1.9366	3.5384
2	−7.0789	4.8916	4.7722	0.6845	19.7565	−19.2092
3	−5.7115	−3.4839	−3.8846	−0.3494	−15.9011	14.8522
4	−2.3494	0.0361	−1.3206	0.1776	−5.0981	−0.0436
All	−16.7539	0.1147	0.1586	0.2099	1.0514	0.1771

Table 11 Forces and torques (deployed configuration, set 1, thruster 3; $M = F_T \times 1m$)

T_w	F_X/F_T, %	F_Y/F_T, %	F_Z/F_T, %	M_X/M, %	M_Y/M, %	M_Z/M, %
273 K	−1.3621	−0.7132	−0.8297	−0.1380	−2.9690	2.8520
167 K	−1.3492	−0.6575	−0.7718	−0.1274	−2.7316	2.6220

Table 12 Maximum convective heat fluxes, W/m^2(deployed configuration, set 1, thruster 3)

T_w	Yoke		1 SA		2 SA		3 SA	
	Back	Edge	Back	Edge	Back	Edge	Back	Edge
273 K	6.0	3.3	11.9	5.0	12.9	30.9	11.0	38.1
167 K	7.8	4.3	13.8	6.3	14.6	34.7	12.2	40.9

Table 13 Forces and torques for the diffuse model without energy accommodation (set 1; $M = F_T \times 1m$)

Thruster	F_X/F_T, %	F_Y/F_T, %	F_Z/F_T, %	M_X/M, %	M_Y/M, %	M_Z/M, %
1	−0.1866	−0.2100	0.0784	−0.0423	0.1495	0.6967
2	−1.6542	1.3825	1.4165	0.0410	5.6330	−5.5339
3	−1.4102	−1.1583	−1.2855	−0.2369	−5.0250	4.8642
4	−0.3550	0.0235	−0.3568	0.0345	−1.2390	0.0863
All	−4.0233	−0.0643	−0.1744	−0.2549	−0.5407	0.4972

factor of 2, and the difference is smaller for all edges, except the edge of the first panel of the solar array. Molecules collide with the edges at small incidence angle, and the model predicts larger energy accommodation for such collisions. Note that when four thrusters fire, heat fluxes are lower than the sum of all the single thruster contributions. This is due to the interaction of thruster plumes and it was also observed for diffuse reflection.

2. *Cook and Hoffbauer Model*

TsAGI determined that the parameters of the Nocilla model for high-speed molecular beam consist of N_2 and O_2. This corresponds very well to the LEO environment. The plume exhausted from the Aeolus thrusters is characterized by lower velocity (1.5–2.2 km/s) and another chemical composition. Cook [18] conducted experiments with beam velocities from 1.6 to 4.1 km/s and molecules typical for plume thruster flows: H_2, N_2, CO, and CO_2. He measured forces exerted on surfaces of Kapton, SiO_2-coated Kapton, solar array material, and white paint Z-93. Cook and Hoffbauer [19] developed another way to determine the parameters of the Nocilla model. The forces are defined with reduced force coefficients obtained from experimental data:

$$p_{sn} = (f_n - \cos\theta_i)p_i \tag{5}$$

$$p_{st} = (\sin\theta_i - f_t)p_i \tag{6}$$

For the last free parameter of the Nocilla model, they assumed that accommodation coefficients of kinetic energy defined for averaged squared velocities and squares of averaged velocities are equal, $\epsilon = \epsilon'$.

$$\epsilon = \frac{\bar{v}_i^2 - \bar{v}_s^2}{\bar{v}_i^2 - 4kT_w/m}, \qquad \epsilon' = \frac{\bar{v}_i^2 - \bar{v}_s^2}{\bar{v}_i^2 - \pi kT_w/2m} \tag{7}$$

where $v_s = v_i\sqrt{(f_t - \sin\theta_i)^2 + (f_n - \cos\theta_i)^2}$ and terms with T_w are for molecules scattered from the surface diffusively with complete energy accommodation. Using equations for forces and energy flux, Cook and Hoffbauer [19] derived a system of two nonlinear equations to find the value of S. Taking S_n and S_t as independent parameters, this system can be reduced to one nonlinear equation for S_n:

$$B\chi\left\{e^{-S_n^2}\left(2 + S_n^2\right) + \sqrt{\pi}S_n\left(\tfrac{5}{2} + S_n^2\right)(1 + erfS_n)\right\} = (C - A)\left\{S_n e^{-S_n^2} + \sqrt{\pi}\left(\tfrac{1}{2} + S_n^2\right)(1 + erfS_n)\right\}^2 \tag{8}$$

where $\chi = e^{-S_n^2} + \sqrt{\pi}S_n(1 + erfS_n)$, $A = v_i^2(\sin\theta_i - f_t)^2$, $B = v_i^2(f_n - \cos\theta_i)^2$, and $C = \bar{v}_i^2 - \epsilon'\left(\bar{v}_i^2 - 4kT_w/m\right)$. T_s and S_t are found with

$$2(k/m)T_s = \frac{\left\{S_n e^{-S_n^2} + \sqrt{\pi}\left[(1/2) + S_n^2\right](1 + erfS_n)\right\}^2}{B\chi^2} \tag{9}$$

$$S_t = \sqrt{A/2(k/m)T_s} \tag{10}$$

However, an iterative process is still needed to solve Eq. (8), which requires more CPU time than with the TsAGI model. This is important for the DSMC method, because the total number of molecular collisions with a surface was up to 10^8 in the course of computation.

Figure 9 shows reduced coefficients obtained with the TsAGI model and by Cook [18]. The TsAGI model gives a normal force

Table 14 Parameters of the TsAGI model (taken from [16])

Material	a_n	b_n	a_t	b_t
Solar array	0.17	0.09	−0.10	−0.08
White enamel	0.07	0.10	−0.01	0.16

coefficient close to Cook's data, the difference is less than 10%, which is an error bar of Cook's experimental data. Despite that TsAGI performed measurements for N_2 and O_2 only, the model also well predicts a normal force coefficient for H_2. The coefficient is slightly above Cook's data, but the difference is within 10%. The TsAGI prediction of tangential force coefficient agrees well with Cook's data, up to an incidence angle of 45 deg, then they deviate. This is due to a linear approximation of forces used in the TsAGI model. Angular distributions of scattered molecules obtained with the TsAGI and Cook and Hoffbauer [19] models are very different, and the difference increases with incidence angle (Fig. 10).

3. *Combined Model*

Let us develop a model that combines the best features of the preceding models. Assuming that the TsAGI model gives more realistic angular distribution because it is based on corresponding measurements, Eq. (4) is chosen to define S_n. This also allows us to avoid an iterative process.

Cook [18] made measurements only for two values of incidence velocity and room wall temperature $T_w^{\exp} = 295$ K, and normal force coefficient depends on incident velocity, except for the solar array material (Fig. 11a shows the coefficients for Z-93). A decrease of the velocity shifts up a dependence of the coefficient vs incidence angle by a constant value. For the present plume analysis, a wall temperature is not equal to $T_w^{\exp}$ and spectrum of velocity is continuous. The question is how to extrapolate experimental data for f_n to another value of wall temperature and lower velocity than corresponding values in Cook's experiment.

To use Cook's [18] data, we assume that this shift is due to a wall temperature effect that is stronger for a smaller incident velocity. Therefore, an equation for p_{sn} is used in the following form:

$$p_{sn} = (f'_n - \cos\theta_i)p_i + \beta\sqrt{(\pi/2)mkT_w} \tag{11}$$

where $f'_n = f_n - \beta\sqrt{(\pi/2)(k/m)T_w^{\exp}}/v_i^{\exp}$. β is constant and it is zero for the solar array material for all considered gases, and for Z-93, $\beta = 0.6$ and 0.95 for H_2 and N_2, respectively. Perhaps β should be a function of incident velocity and Eq. (11) should converge to diffuse reflection with complete energy accommodation ($\beta = 1$) when the velocity is going to zero. However, to define a better approximation of β, additional experimental data are needed, especially for another value of wall temperature. Modified normal force coefficients f'_n are independent of incident velocity, and a difference between N_2 and H_2 curves is almost constant [about 0.15 (Fig. 11b)]. The TsAGI model predicts values that are located between N_2 and H_2 curves, except 0 and 85 deg, when they coincide with N_2 and H_2, respectively.

For a tangential force, we take Eq. (6), because for the Aeolus plume analysis, we need accurate data for any incidence angle, and experimental data show negligible effect of incidence velocity on f_t for solar arrays and Z-93. Values of f'_n and f_t between experimental points are interpolated with second-order polynomials. Fractions of H_2O and NH_3 are negligibly small, and N_2 data are used for these gases.

Figure 10 also shows angular distributions obtained with the combined model. For a small incidence angle, the model predicts angular distribution of N_2 close to the TsAGI prediction, and for a large angle, a combined model prediction is much closer to the TsAGI results than to the Cook and Hoffbauer [19] distribution. The situation is the opposite for H_2 distributions, for which the combined model gives distributions very similar to the Cook and Hoffbauer results. Plume impingement analysis was perform with a combined model, and corresponding DSMC results are listed in Tables 17 and 18. Scattering from Z-93 is nearly diffuse, and the TsAGI and combined models give similar forces and torques. The largest difference between these model predictions is observed when a plume impinges onto the front side of solar arrays (firing of the second thruster). A contribution of the second thruster also affects results when four thruster fire simultaneously. The combined model predicts higher heat fluxes, because scattered molecules have smaller energy for this model (cf. Tables 16 and 18). The heat fluxes are still lower than the corresponding values predicted by diffuse reflection with complete energy accommodation (cf. Tables 5 and 18).

VIII. Conclusions

Numerical analysis of plume impingement for the Aeolus spacecraft was done with a multizone approach based on successive application of continuum (Navier–Stokes equations) and kinetic (the DSMC method) approaches to accurately predict plume flow and plume impingement. Computations were performed with the Navier–Stokes solver CFD-FASTRAN and the DSMC-based SMILE.

Two sets of chemical composition were considered for the 5-N MONARC thruster: 60% and complete dissociation of ammonia. It was shown that an incomplete dissociation of ammonia leads to higher heat fluxes and absolute values of forces and torques. A thrust vector is tilted by 15 deg in the Z plane away from the solar array to reduce plume impingement effects. Computations with zero angle have showed that a decrease of thrust angle does not reduce the total thrust loss and leads to higher heat fluxes by a factor of 3–7.

DSMC computations of plume flow around configurations with stowed and deployed solar arrays show that the flow is very rarefied in the vicinity of the solar array and the continuum approach is not

Table 15 Forces and torques (TsAGI model; $T_w = 273$ K and $M = F_T \times 1m$)

Thruster	F_X/F_T, %	F_Y/F_T, %	F_Z/F_T, %	M_X/M, %	M_Y/M, %	M_Z/M, %
1	−0.1787	−0.1648	0.0697	−0.0296	0.1383	0.5396
2	−1.4338	1.1296	1.1599	0.0345	4.5295	−4.4477
3	−1.3065	−0.8865	−0.9888	−0.1618	−3.7094	3.5897
4	−0.3398	0.0547	−0.2770	0.0220	−0.9159	−0.0596
All	−3.6755	0.0236	−0.0810	−0.2013	0.0835	−0.0792

Table 16 Maximum convective heat fluxes, W/m^2 (TsAGI model; $T_w = 273$ K)

	Yoke			1 SA			2 SA			3 SA		
	Front	Back	Edge	Front	Back	Edge	Front	Back	Edge	Front	Back	Edge
1	0.09	1.44	96.4	−0.01	1.40	38.39	−0.01	0.84	24.30	−0.01	0.31	10.04
2	6.58	0.04	3.89	5.10	0.00	7.22	5.18	0.00	49.46	3.31	0.00	43.71
3	0.04	3.86	1.49	0.00	6.52	2.67	0.00	6.98	26.83	0.00	6.07	36.23
4	0.08	3.17	34.19	0.00	4.61	22.95	0.00	4.00	23.47	0.00	1.71	13.63
All	5.82	4.52	93.52	2.77	6.18	40.30	1.60	6.39	74.42	1.70	5.84	61.10

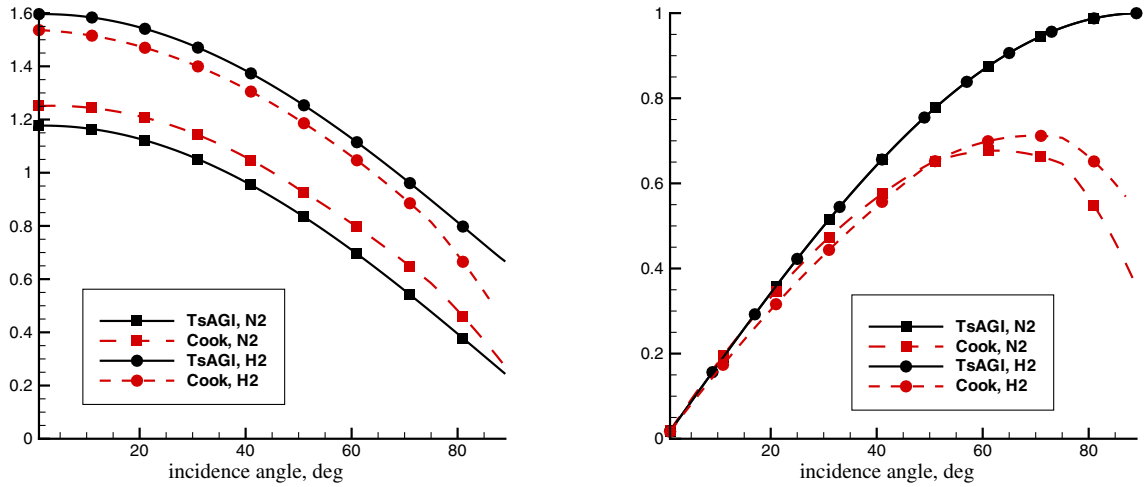

a) Normal force b) Tangential force

Fig. 9 Reduced force coefficients for the TsAGI model and Cook's data [18] for solar array material ($T_w = 295$ K, $v_i = 3180$ and 2590 m/s for N_2 and H_2, respectively).

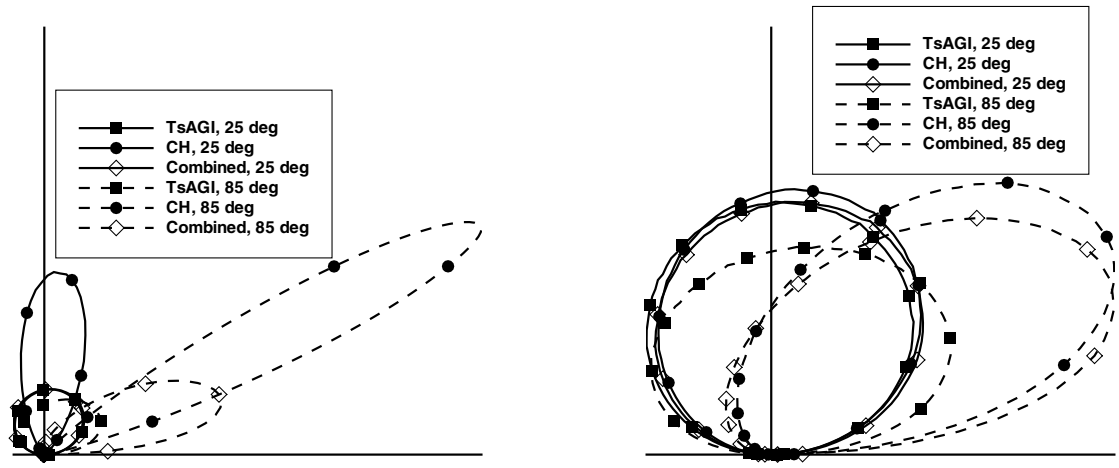

a) N_2, $v_i = 3180$ m/s b) H_2, $v_i = 2590$ m/s

Fig. 10 Angular density distributions for solar array material (solid line is $\theta_i = 25$ deg, dashed line is $\theta_i = 85$, and $T_w = 295$ K).

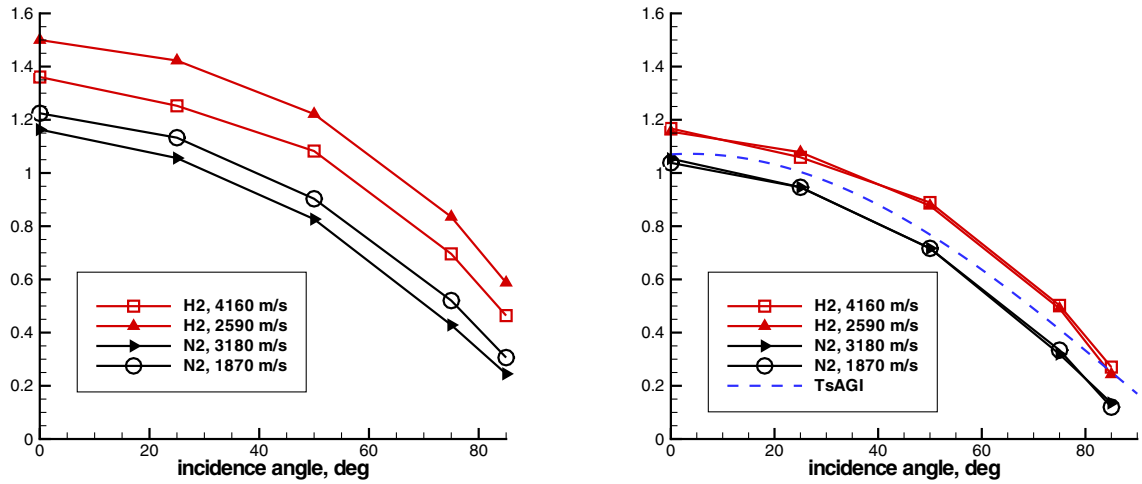

a) Cook [18] data, $T_w = 295$ K b) Modified coefficients f_n'

Fig. 11 Reduced normal force coefficients for Z-93.

valid. However, molecular collisions are still important, especially when few thrusters fire. This leads to values of forces, torques, and convective heat fluxes that are different from a sum of corresponding values for single thruster firings.

A convective heat flux is more important for the stowed configuration, due to the small distance between the thrusters and the solar array. Maximum heat flux, about 350 W/m^2, locates on an edge of the third panel of the solar array. For deployed configuration,

Table 17 Forces and torques for the combined model ($T_w = 273$ K and $M = F_T \times 1m$)

Thruster	F_X/F_T, %	F_Y/F_T, %	F_Z/F_T, %	M_X/M, %	M_Y/M, %	M_Z/M, %
1	−0.2081	−0.1419	0.0729	−0.0214	0.1671	0.4666
2	−1.1177	0.9449	0.9775	0.0243	3.7212	−3.6432
3	−1.3507	−0.7591	−0.8643	−0.1362	−3.1297	3.0146
4	−0.3678	0.0793	−0.2366	0.0182	−0.7583	−0.1775
All	−3.4227	−0.0591	−0.1360	−0.1837	−0.3202	0.4636

Table 18 Maximum convective heat fluxes for the combined model, W/m^2 ($T_w = 273$ K)

	Yoke			1 SA			2 SA			3 SA		
	Front	Back	Edge	Front	Back	Edge	Front	Back	Edge	Front	Back	Edge
1	0.11	4.66	119.7	0.12	4.55	56.66	0.12	2.92	27.27	0.04	1.13	11.24
2	9.17	0.03	5.67	11.07	0.00	9.83	10.81	0.00	58.43	6.58	0.00	49.57
3	0.05	5.20	2.44	0.00	9.69	3.92	0.00	11.02	31.12	0.00	9.74	39.83
4	0.04	6.70	42.47	0.08	8.98	34.84	0.08	7.32	28.92	0.04	3.30	14.71
All	9.35	10.13	119.37	10.83	14.98	55.99	10.58	14.93	93.60	7.05	11.88	75.05

the highest values of heat flux ($\sim$100 W/m^2) are observed on the edges of the yoke and first solar array panel. Exact numerical methods are crucial for the analysis. For example, an application of NS equations and the free-molecular method for the deployed SA configuration underpredicts mechanical and heat loads, the latter by a factor of 2.

Flow regime is nearly free-molecular at the solar array, and gas/surface interaction is very important for the plume impingement analysis. The Nocilla model is more advanced than the gas/surface interaction model, compared with diffuse reflection, and there are different ways to determine the model parameters. TsAGI developed a determination that takes into account incidence angle, energy of incident molecule, and the properties of a surface [15,16]. An application of this model gives significantly smaller heat fluxes than diffuse reflection with complete energy accommodation. Forces and torques are about an average of corresponding values obtained from diffuse reflection with and without complete energy accommodation.

TsAGI conducted experiments of the interaction of a high-speed molecular beam (consisting of N_2 and O_2) with engineering surfaces. The velocity and chemical composition are typical for LEO, however, plume flows have smaller velocities and other chemical compositions. Cook [18] performed force measurements for beam parameters typical for plume flow, and comparison between his data and the TsAGI prediction showed that the TsAGI model predicts values of reduced normal force coefficient that are similar to Cook's data (a difference is within an error of the experimental data). Tangential force coefficients are very close to Cook's data, up to an angle of 45 deg, then they deviate. The main difference between the TsAGI and Cook and Hoffbauer [19] models is observed for an angular distribution of scattered molecules: the Cook and Hoffbauer model gives a very narrow distribution for N_2.

A new method for determining the Nocilla model parameters was developed using TsAGI approximation for normal velocity ratio vs incidence angle and force measurements performed by Cook [18]. An application of this model to the Aeolus case gives values of forces and toques similar to corresponding values obtained with the TsAGI model, except in a case when a plume impinges onto the front side of the solar array. The model predicts heat fluxes higher than the TsAGI model prediction, because scattered molecules have smaller energy for this model. However, heat fluxes are still lower than corresponding values obtained from diffuse reflection with complete energy accommodation, especially for the front side of the solar array.

Appendix A: Numerical Accuracy of DSMC Computations

The DSMC method deals with model particles, and a grid is used to implement an efficient algorithm to choose a particle pair for a collision. Therefore, the user should pay attention to particle and grid convergences of the DSMC solution. The majorant frequency scheme of the DSMC method is implemented in SMILE, and this scheme allows one to use a small number of particles for accurate modeling of the relaxation process. In our case, the number of model particles was kept nearly constant (about four) in each cell. When the number of particles is changed, a grid is modified accordingly; we will further discuss particle/grid convergence, keeping in mind that they are bound.

I. Stowed SA Configuration

Computations of plume flow around the configuration with stowed solar arrays were the heaviest from a CPU viewpoint, and it was not possible to use a standard approach such as a successive grid refinement, because the total number of cells was about 14×10^6, which was the limit of computer resources used. Fortunately, due to a thruster position against the solar array, an axisymmetric assumption gives very realistic prediction of maximum values of heat fluxes. Performed axisymmetric computation predicts almost the same values of heat fluxes as the 3-D solution.

II. Deployed SA Configuration

For the configuration with deployed solar array, the DSMC zone was divided into two subzones. In the first subzone, an axisymmetric modeling was performed and all requirements to numerical parameters of the DSMC method were satisfied. Three-dimensional computations in the second subzone were performed for three sets of grid/number of model particles. The p1 grid has 2×10^6 cells and 6×10^6 model particles. The p2 grid has double the number of cells and particles and the total number of cells and model particles are multiplied by a factor of 8 for the p8 grid. No significant difference for forces, torques, and convective heat fluxes is observed (Tables A1

Table A1 Forces and torques (deployed configuration, set 1, thruster 3; $T_w = 273$ K and $M = F_T \times 1m$)

Grid	F_X/F_T, %	F_Y/F_T, %	F_Z/F_T, %	M_X/M, %	M_Y/M, %	M_Z/M, %
p1	−1.3621	−0.7132	−0.8297	−0.1380	−2.9690	2.8520
p2	−1.3636	−0.7138	−0.8303	−0.1380	−2.9715	2.8543
p8	−1.3607	−0.7139	−0.8298	−0.1378	−2.9695	2.8535

Table A2 Maximum convective heat fluxes, W/m^2 (deployed configuration, set 1, thruster 3; $T_w = 273$ K)

Grid	Yoke			1 SA			2 SA			3 SA		
	Front	Back	Edge	Front	Back	Edge	Front	Back	Edge	Front	Back	Edge
p1	0.02	6.0	3.3	0.01	11.9	5.0	0.01	12.9	30.9	0.01	11.0	38.1
p2	0.06	6.3	3.5	0.01	12.1	5.0	0.01	13.1	31.0	0.01	11.2	38.3
p8	0.03	6.4	3.8	0.01	12.1	5.0	0.01	13.0	31.2	0.01	10.9	38.0

and A2). Therefore, computations of a single thruster plume were performed with the p1 grid and four thruster plumes, with the total number of cells and model particles larger by a factor of 4.

Acknowledgments

Thanks go to Rolf Brandt, Gilles Labruyere, Wolfgang Veith (ESA-ESTEC/EOP) and Lionel Marraffa (ESA-ESTEC/TEC-MPA) for involving the author in the project, Ingrid Wysong (U.S. Air Force Research Laboratory) for fruitful discussions on gas/surface interaction, and Paul Pearson (Advanced Operations and Engineering Services Group, B.V.) for the computer resources used for the direct simulation Monte Carlo computations.

References

[1] Ivanov, M. S., Markelov, G. N., and Gimelshein, S. F., "Statistical Simulation of Reactive Rarefied Flows: Numerical Approach and Applications," AIAA Paper 98-2669, Albuquerque, June 1998.

[2] "Aeolus Mechanical Interface Control Document," EADS Astrium, Ltd., Rept. AE.IF.ASU.SC.001, Stevenage, England, U.K., 2004.

[3] Simmonds, Miller, and Nealy, "Tables and Charts of Equilibrium Thermodynamic Properties of Ammonia for Temperatures from 500 to 50000 K," NASA SP-3099, 1976.

[4] Giordano, D., Ivanov, M. S., Kashkovsky, A. V., Markelov, G. N., Tumino, G., and Koppenwallner G., "Application of the Numerical Multizone Approach to the Study of Satellite Thruster Plumes," *Journal of Spacecraft and Rockets*, Vol. 35, No. 4, 1998, pp. 502–508.

[5] Ivanov, M. S., Markelov, G. N., Gerasimov Yu. I., Krylov, A. N., Mishina, L. V., and Sokolov, E. I., "Free-Fight Experiment and Numerical Simulation for Cold Thruster Plume," *Journal of Propulsion and Power*, Vol. 15, No. 3, 1999, pp. 417–423.

[6] Bird, G. A., *Molecular Gas Dynamics and the Direct Simulation of Gas Flows*, Pergamon, New York, 1994.

[7] CFD-FASTRAN, Software Package, Ver. 2003, ESI US Research and Development, Inc., Huntsville, AL, 2004.

[8] Rault, D. F. G., "Methodology for Thruster Plume Simulation and Impingement Effects Characterized by DSMC," AIAA Paper 95-2032, 1995.

[9] Lumpkin, F. E., Stuart, P. C., and Le Beau, G. J., "Enhanced Analysis of Plume Impingement During Shuttle-Mir Docking Using Combined CFD And DSMC Methodology," AIAA Paper 96-1877, 1996.

[10] Nocilla S., "The Surface Re-Emission Law in Free Molecule Flow," *Proceedings of the Third International Symposium on Rarefied Gas Dynamics*, Vol. 1, Academic Press, New York, 1963, pp. 327–346.

[11] Lord, R. G., "Some Further Extensions of the Cercignani-Lampis Gas-Surface Interaction Model," *Physics of Fluids*, Vol. 7, No. 5, 1995, pp. 1159–1161.

[12] Cheoux-Damas, P., Theroude, C., and Gibek I., "Space Engineering Tools for Plume Effects Comparison with Measurements," AIAA Paper 95-2849, 1995.

[13] Collins, F. G., and Knox, E. C., "Parameters of the Nocilla Gas/Surface Interaction Model from Measured Accommodation Coefficients," *AIAA Journal*, Vol. 32, No. 4, 1994, pp. 765–773.

[14] Collins, F. G., and Knox, E. C., "Determination of Wall Boundary Conditions for High-Speed-Ratio Direct Simulation Monte Carlo Calculations," *Journal of Spacecraft and Rockets*, Vol. 31, No. 6, 1994, pp. 965–970.

[15] Musanov, S. V., Nikiforov, A. P., Omelik, A. L., and Freedlender, O. G., "Experimental Determination of Momentum Transfer Coefficients in Hypersonic Free Molecular Flow and Distribution Function Recovery of Reflected Molecules," *Proceedings of the Thirteenth International Symposium on Rarefied Gas Dynamics*, Vol. 1, Plenum, New York, 1985, pp. 669–676.

[16] Freedlender, O. G., and Nikiforov, A. P., "Modelling Aerodynamic Atmospheric Effects on the Space Vehicle Based on Test Data," 2nd International Symposium on Environmental Testing for Space Programmes, ESA Paper WPP-066, 1993.

[17] Markelov, G. N., Kashkovsky, A. V., and Ivanov, M. S., "Space Station Mir Aerodynamics Along the Descent Trajectory," *Journal of Spacecraft and Rockets*, Vol. 38, No. 1, 2001, pp. 43–50.

[18] Cook, S. R., "Molecular Beam Measurements of Absolute Momentum Accommodation on Spacecraft Surfaces Using a Specialized Torsion Balance," Ph.D. Thesis, Univ. of Texas at Austin, Austin, TX, 1995.

[19] Cook, S. R., and Hoffbauer, M. A., "Nocilla Model Parameters Obtained from Forces Exerted on Surfaces by Molecular Beams," *Journal of Spacecraft and Rockets*, Vol. 34, No. 3, 1997, pp. 379–383.

I. Boyd
Associate Editor